Title
In situ Microscopy Studies of Growth Kinetics of Monolayer Graphene on Pd(111)

Author
Mok, Hoi Sing

Publication Date
2013

Peer reviewed|Thesis/dissertation

UNIVERSITY OF CALIFORNIA

Los Angeles

In situ Microscopy Studies of Growth Kinetics of Monolayer Graphene on Pd(111)

A thesis submitted in partial satisfaction

of the requirements for the degree Master of Science

in Materials Science and Engineering

by

Hoi Sing Mok

ABSTRACT OF THE THESIS

In situ Microscopy Studies of Growth Kinetics of Monolayer Graphene on Pd(111)

by

Hoi Sing Mok

Master of Science in Materials Science and Engineering

University of California, Los Angeles, 2013

Professor Suneel Kodambaka

The objective of my thesis is to use in situ low-energy electron microscopy (LEEM) and investigate the growth kinetics of monolayer graphene domains and the role of oxygen on graphene layer formation. In order to determine the growth mechanisms, LEEM images were acquired during graphene layer formation via surface segregation of carbon on single-crystalline Pd(111). Electron reflectivities and graphene growth rates were measured as a function of annealing temperature, time, and oxygen partial pressure. From the time-dependent variations in surface work function and graphene growth area, possible rate limiting processes controlling graphene layer formation were identified. Introduction of oxygen during graphene growth resulted in a lowering of graphene growth rate. And, the measured rates of graphene growth decreased with increasing oxygen partial pressure. These results provide new insights into the graphene growth kinetics and the role of oxygen.

The thesis of Hoi Sing Mok is approved.

Ya-Hong Xie

Chi On Chui

Suneel Kodambaka, Committee Chair

University of California, Los Angeles

2013

Table of Contents

List of Figures

Acknowledgements

Dr. Kevin McCarty and his group for the opportunity to do research at Sandia National Labs and for all the assistance they provided, and Professor Cristian Ciobanu and his group for performing density function theory calculations.

I would also like to thank Dr. Yuya Murata and Chilan Ngo for when I first started on my research, and all the support and advice over the years.

Lastly to thank Professor Suneel Kodambaka for everything he has done to mentor me, as without his expertise and supervision on my projects, I would not have been able to accomplish this work.

CHAPTER 1: INTRODUCTION

1.1 Graphene Background and Motivation

Monolayer-thick crystalline sheets of carbon atoms in a hexagonal lattice, commonly known as graphene, has attracted substantial attention since its discovery.[1] Graphene is the basic structural unit for various carbon allotropes of different dimensionalities. Figure 1 depicts a few of these variations, which include stacked graphene sheets (graphite), rolled up sheets (carbon nanotubes), and folded three-dimensional (3D) structures (fullerenes).[2] The properties of these allotropes vary substantially from one another.

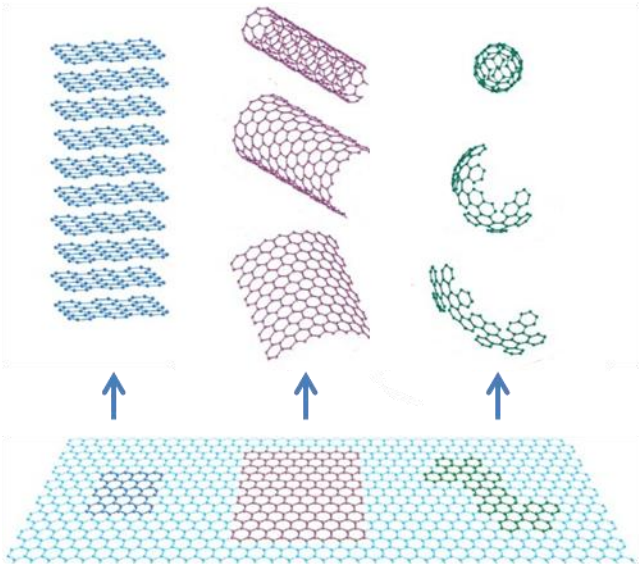

Figure 1. Schematic representation of different carbon allotropes, adapted from Ref 1.

In free-standing graphene layers, carbon atoms undergo sp^2 hybridization between one s-orbital and two p-orbitals to form 3 σ bonds per carbon atom, with a separation of 1.42 Å.[3] The remaining unaffected p-orbitals, which are perpendicular to the planar structure, form half-filled π bands with neighboring atoms.

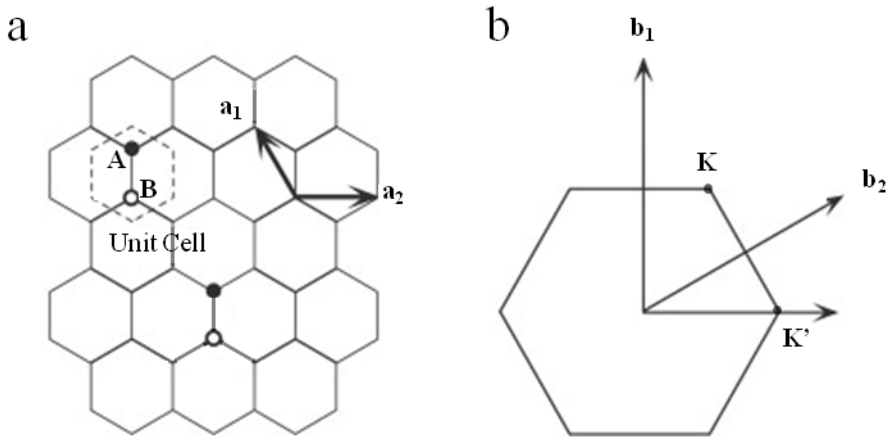

Figure 2. (a) Real space lattice of graphene. Two atoms, denoted by A and B, make up the unit cell. Primitive lattice unit vectors are given by $\overrightarrow{a_1}$ and $\overrightarrow{a_2}$. (b) First Brillouin zone of graphene. The reciprocal lattice unit vectors are designated by $\overrightarrow{b_1}$ and $\overrightarrow{b_2}$, and the Dirac points are located at K and K'. Adapted from Ref. 4.

The unit cell of graphene, shown in Figure 2a, consists of two atoms with real space vectors:

$$\overrightarrow{a_1} = \frac{a}{2}\left(3, \sqrt{3}\right) \text{ and } \overrightarrow{a_2} = \frac{a}{2}\left(3, -\sqrt{3}\right),$$

where $\overrightarrow{a_1}$ and $\overrightarrow{a_2}$ are the primitive lattice vectors. The first Brillouin zone is shown in Figure 2b and the reciprocal lattice vectors are:

$$\overrightarrow{b_1} = \frac{2\pi}{3a}\left(1, \sqrt{3}\right) \text{ and } \overrightarrow{b_2} = \frac{2\pi}{3a}\left(1, -\sqrt{3}\right).$$

Of particular interest are the points *K* and *K'*, located at:

$$\left(\frac{2\pi}{3a}, \frac{2\pi}{3\sqrt{3}a}\right) \text{ and } \left(\frac{2\pi}{3a}, -\frac{2\pi}{3\sqrt{3}a}\right).$$

These locations are the valley points in the graphene band structure, around which charge carriers exhibit unique behavior, with a linear energy dispersion, that forms a cone in 3D.[3] This Dirac cone, as pictured in Figure 3, highlights the intersection between the conduction and valence bands, commonly referred to as the Dirac point, which is also the location of the Fermi

level. The lack of an energy gap between the bands is a defining feature of free-standing graphene, although it has been demonstrated that a band gap can be introduced by breaking symmetry in the lattice, for example, via stacking bilayers[5] or by growing graphene on strongly interacting substrates.[6]

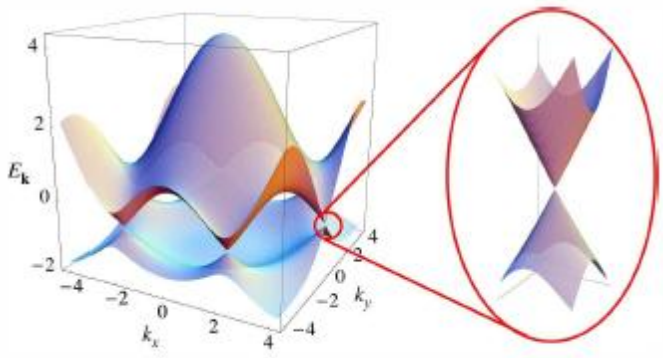

Figure 3. 3D diagram of graphene band structure, with a magnified view of the Dirac cone. Adapted from Ref. 2.

In addition to the absence of a band gap, free-standing graphene has been found to display other novel material properties, for example, outstanding mechanical, thermal, and electrical properties, including high electron mobility[7] and a tunable band gap.[8] Charge carriers near the Dirac point behave as massless particles,[3] which possess a high Fermi velocity of 10^6 m/s. Free-standing graphene also has an electron mobility of 200,000 $cm^2V^{-1}s^{-1}$ at 5 K. At room temperature, the mobility of substrate-supported graphene reduces to 15,000 $cm^2V^{-1}s^{-1}$. This value is still significantly higher than the electron mobility of Si (1400 $cm^2V^{-1}s^{-1}$).[7] Furthermore, the mean free path of electrons in graphene is of the order of micrometers,[9] another highly desirable trait for electronics.

Among a wide variety of potential applications of graphene, high performance transistors[10] and transparent conductors[11] are considered promising. Motivated by these prospects, recent research

efforts have focused on the large-scale growth of graphene layers with precisely controlled thicknesses. Graphene sheets grown on most substrates exhibit polydomain structure even on lattice-matched substrates due to weak graphene-substrate interactions. Due to the fact that electronic characteristics of graphene-based devices can vary with domain structure,[12] it is desirable to eliminate domain boundaries or control their structure.[13] Moreover, graphene layers that are synthesized on metals need to be transferred onto non-conducting substrates for the fabrication of electronic devices. Wet-chemical etching and nanolithography techniques are primarily used to remove and transfer the graphene layers from the metal substrates. This approach involves spin coating of a layer of polymethyl methancrylate (PMMA) to act as a structural support during the etching of the substrate by nitric acid or iron (III) chloride solutions.[14] The graphene layer then floats to the surface and can be transferred onto a dielectric material for device fabrication or characterization. This process can introduce contaminants and wrinkles in the layers, and often the transferred graphene layer properties are not reproducible.

While remarkable progress has been achieved over the past decade in the synthesis and fabrication of graphene-based devices, several aspects concerning the controlled growth of graphene layers with desired layer thickness and domain orientation are not yet clear. Detailed understanding of these details can help further improve graphene layer quality and hence develop high-performance graphene-based devices.

1.2 Graphene Growth Techniques

Among the various methods available to synthesize graphene, probably the simplest process is the mechanical exfoliation of pyrolytic graphite. First demonstrated by Geim and Novoselov in 2004, this method involves the use of adhesive tape to peel apart graphite layers that are weakly

held together by van der Waals forces.[15] By repeatedly peeling a piece of graphite, individual graphene layers can be isolated, as shown in Figure 4, and can be transferred to a separate substrate, typically oxidized Si wafers, for further characterization. For sufficiently thin SiO_2 films, of either 300 or 90 nm, graphene contrast with the substrate is maximized at 12%, and the optical path difference between various layers can be used to identify graphene layers of different thicknesses by their characteristic color.

While the mechanical exfoliation approach is fairly inexpensive and the samples produced by this method are of high quality, it is not a scalable process for the production of large-area graphene. Limited flake size and reproducibility in achieving precisely controlled thicknesses are major drawbacks for the ultra-large scale integration of any potential graphene based device. Hence, this method is generally restricted to laboratory-scale experimental studies.

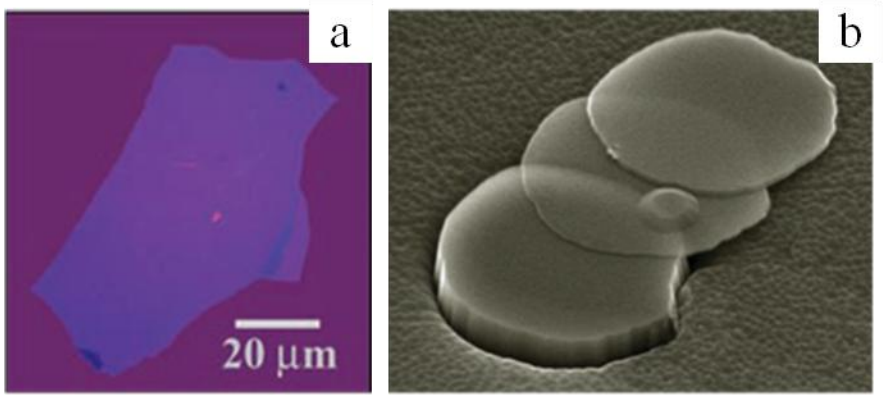

Figure 4. (a) Optical image of a graphene layer transferred onto an SiO_2 substrate. (b) SEM image of graphite layers exfoliated from a graphite sample. Adapted from Ref. 15.

Large-area graphene layers are commonly grown by several methods, including: 1) chemical vapor deposition (CVD) of carbon via pyrolytic cracking of hydrocarbons onto transition metals at high temperatures,[16] 2) segregation of carbon atoms during cooling of carbon containing substrates,[17] and 3) high temperature annealing of SiC in vacuum or inert atmospheres.[18] Out of

these methods, high quality graphene layers can be produced via epitaxial growth on Si- or C-terminated SiC substrates by annealing the wafers at high temperatures, typically above 1100 ^{o}C. In this process, Si atoms sublimate from the substrate surface leaving behind C atoms which rearrange into graphitic layers.[18] This approach enables fabrication of devices directly on the substrate, as SiC is a wide band gap material, thus eliminating the need for the chemomechanical transfer of graphene, an intrinsically unreliable process, as mentioned in the section 1.1.

Previous studies have shown that graphene growth kinetics and its properties depend on the surface termination of SiC: Si terminated SiC(0001) and C terminated SiC($000\bar{1}$).[19,20] On the C-face, graphene grows at a faster rate than on the Si-face, and is weakly bonded to the substrate. The high nucleation rate and diffusivity of C atoms to the nucleation sites below the first graphene layer lead to small domain sizes and multilayer growth.[21,22] In contrast, relatively larger monolayer graphene domains form on Si-face SiC and are bound strongly to the substrate.[22] Consequently, electronic properties of graphene grown on each of these faces also varies: as electron mobility in graphene on C-face is superior to that measured in graphene grown on Si-face SiC(0001) substrates.

Another popular method to obtain large-area graphene is through CVD of carbon on heated metal substrates. In this process, the metal surface catalyzes the pyrolytic cracking of hydrocarbons. Factors influencing the growth and quality of the graphene layers include the solubility of C in the substrate, crystal structure and lattice mismatch, and experimental parameters (temperature and flux) of the system.[23] A number of different substrates have been used to grow graphene, including Cu,[16] Ni,[17] Pt,[24] Ru,[25] Ir, [26] Rh,[27] and Re.[28] In a typical growth experiment, a substrate, such as Ni, is heated to high temperatures, (~1000 ^{o}C) in an inert

atmosphere, and exposed to a flow of hydrocarbon (for example, methane), hydrogen, and argon gas mixture.[14] Subsequent annealing and cooling rates then dictate the morphology and thickness of the graphene layers that are formed from the deposited carbon atoms.[29] Once growth is completed, the graphene films are removed from the substrate using the transfer processes described in the previous section for further characterization and device fabrication.

1.3 Oxygen Intercalation

While there has been considerable progress in achieving large-area growth of graphene on metals, the process of transferring graphene layers to insulating substrates has not yet been well developed for large-scale, reproducible device fabrication. A possible alternative to PMMA wet transfer is by selective reactions at the graphene-metal interface, namely decoupling of the graphene layer via intercalated oxygen. Exposure to O_2 at high temperatures causes etching of graphene edges and wrinkles,[30] but at lower temperatures, oxygen atoms can diffuse under the graphene layers. For example, it has been demonstrated for graphene grown on SiC(0001) that selective oxidation below the layers decouples the graphene from the substrate.[20] Oxygen intercalation has also been observed in graphene on Ru(0001)[5] and Ir(111)[6] substrates; intercalated oxygen has been shown to modify the substrate-graphene interaction, leading towards a transition of the electronic band structure of graphene to resemble that of free-standing graphene.[5] In addition, introduction of intercalated oxygen enables stress relaxation in graphene layers on Ru(0001), achieved by the formation of a wrinkle network, as shown in Figure 5.[31] Oxygen-induced changes in the graphene layers can be observed through scanning tunneling microscopy (STM) and low-energy electron microscopy (LEEM) and verified using

photoelectron spectroscopy. This approach is a promising method to separate graphene from the metal substrate with a greater degree of control in comparison to wet transfer methods.

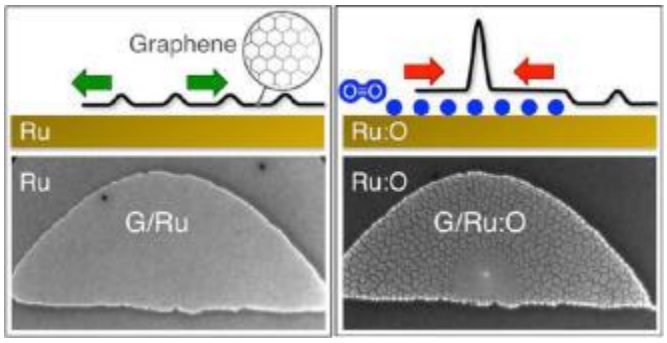

Figure 5. (Top) Schematic of graphene film on Ru(0001) before (left) and after (right) intercalation of oxygen atoms. (Bottom) Bright field LEEM images of graphene in UHV and after oxygen intercalation. Adapted from Ref. 31.

1.4 Mechanisms of Graphene Growth on Metals

Majority of the existing literature on graphene delves with large-area growth and fabrication of graphene-based devices. Relatively far fewer studies focused on the graphene growth mechanisms. Among the existing literature, systematic studies of graphene growth have been carried out on a few metal substrates[32] including Ru(0001)[33], Ir(111)[26], Pt(111)[34], Ni(111),[35] and Cu.[36] The kinetics of graphene growth on metal substrates depends on the solubility of carbon in the metal. For example, CVD of graphene on Cu, which has a low carbon solubility of 0.008 wt.% at ~ 1084 ^{o}C,[37] is a self-limiting process, dictated by the rate of pyrolytic cracking of hydrocarbons[23] and yields monolayer or few layer graphene. In comparison, Ni has a relatively higher solubility for carbon (~ 1.3 wt.% at 1000 ^{o}C), which causes deposited carbon to dissolve into the bulk metal and segregate on the surface during cooling to form graphene. Li *et al.*,[38] used carbon isotopes to determine carbon diffusion pathways during the growth of graphene on Cu and Ni substrates. In these experiments, the substrates were sequentially exposed to methane gases containing two C isotopes ($^{12}CH_4$ and $^{13}CH_4$) and the resulting graphene composition was

determined using Raman spectroscopy. From their experiments, two possible pathways, as shown in Figure 6, were identified: 1) dissolution of C into the bulk substrates with high C solubility and random distribution of isotopes during segregation to the surface and 2) formation of graphene from adsorbed C on low solubility substrates. On substrates such as Ru and Ir, monolayer graphene grows layer by layer[25] via the attachment of C adatom clusters.[39] For growth via surface segregation of C atoms dissolved in the bulk of the metal,[40] the rate limiting step controlling the process is diffusion of C from the bulk to surface.[41] The outcomes of these studies have helped our understanding of the graphene growth process on different metals. Similar studies of graphene growth on other metals are desirable not only for a better understanding of the underlying mechanisms but also for the development of large-area, single-domain, graphene production technologies.

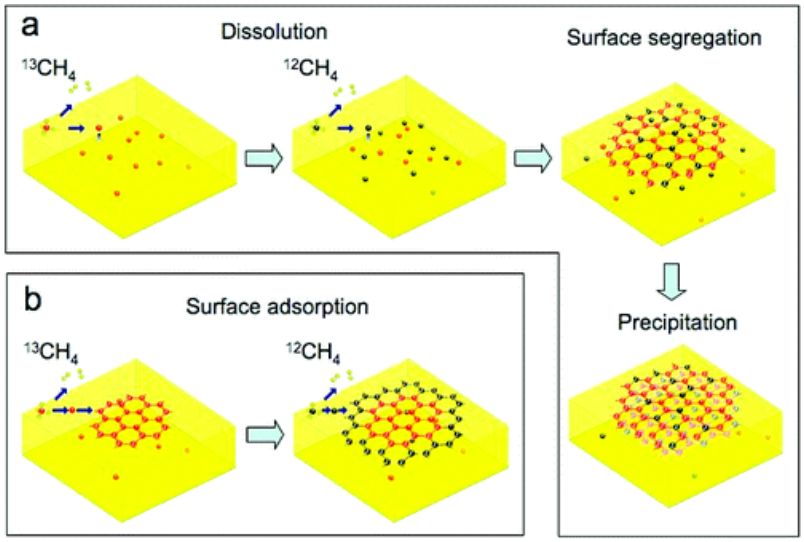

Figure 6. (a) Process flow for graphene growth by segregation. Random distribution of C isotopes will occur during surface segregation. (b) Graphene grown by surface adsorption, where ordering of isotopes may occur in the layer depending on the times at which substrate is exposed to each species. Adapted from Ref. 38.

As part of my thesis, I have chosen to investigate the growth kinetics of graphene on Pd(111). Pd is notable for its role as a catalyst for hydrogenation of unsaturated hydrocarbons.[42] Recent

interest in the growth of graphene on Pd stems from the fact that graphene-Pd contacts have very low contact resistance.[43] This metal has a C solubility of 1.4 wt.% at 750 ^{o}C,[44] which facilitates growth of graphene layers of desired thickness. However, the 9.8% lattice mismatch[45] between Pd(111) and graphene leads to the formation of graphene with multiple domains. Analysis of monolayer graphene grown on Pd(111) using STM has shown that these domains exhibit moiré patterns with large periodicities. Interestingly, graphene on Pd(111) is semiconducting due to a strong graphene-substrate interaction, of the order of ~ 0.13 eV/C atom.[46] LEEM studies of graphene on Pd(111) demonstrated that work function Φ of graphene varies with rotational domain orientation[47] and layer thickness.[48] First principles calculations suggest that the orientation dependent change in Φ is a result of variation in the binding energy of graphene to Pd.[49] Since Φ can dictate whether the metal-graphene interface forms Ohmic or Schottky contact, fundamental understanding of the factors controlling domain formation is desirable. Any prospects gained into the growth kinetics of graphene on Pd(111) may serve to improve the understanding of graphene-Pd contact characteristics and hence graphene-based electronics.

CHAPTER 2: EXPERIMENTAL

2.1 Vacuum System and LEEM

Deposition and growth of materials generally are multi-scale, process-sensitive phenomena involving a complex interplay of thermodynamics and kinetics. Often, trace amounts of residual gases, such as water vapor, oxygen, and carbon monoxide, in a deposition system or common contaminants, such as organic matter, salt, and grease, on substrate surfaces can strongly influence the morphology, composition, and structure of the deposited materials. Hence, clean and well-controlled ambient in the deposition system and carefully-prepared substrate surfaces are desirable for reproducible results and for systematic investigation of the growth kinetics. For solid or vapor phase deposition of materials, ultra-high vacuum (UHV) systems provide a clean environment, free of the residual gases. Vacuum is broadly defined as a pressure less than that of atmospheric pressure (760 Torr) and is split into three regimes: low (760 – 10^{-4} Torr), high (10^{-4} – 10^{-8} Torr), and ultra-high (less than 10^{-8} Torr).

In my thesis work, UHV LEEM is used for the analysis and characterization of the graphene layers. The concept of LEEM was first proposed by E. G. Bauer in 1962, and a functional system was developed by 1985.[50] LEEM is a surface-sensitive imaging technique in which a coherent beam of low-energy electrons (E = 1-100 eV) illuminates the sample surface. The electrons that are specularly reflected from the sample surface are used to obtain real-space images and reciprocal-space diffraction patterns of the sample surface. This technique differs from conventional scanning and transmission electron microscopy techniques (SEM and TEM) in that: 1) the incident electron energies are considerably lower (a few eV) compared to SEM or TEM (tens of kV), 2) specularly reflected electrons provide the information concerning the sample

surface morphology and surface structure, and 3) the illuminating beam and the scattered beam must be separated. LEEM is best-suited for UHV or low-vacuum studies of electrically conducting or semiconducting, crystalline materials with atomically-flat surfaces.[51] A schematic of the LEEM ray diagram for bright field imaging is shown in Figure 7.[52]

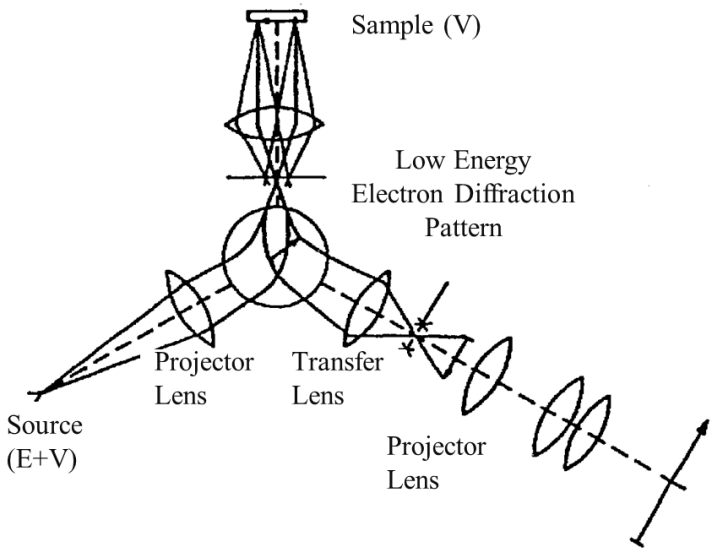

Figure 7. Ray diagram of LEEM operation in bright field imaging mode. Adapted from Ref. 52.

In LEEM, since the low-electron electrons are easily influenced by external fields, the electrons generated from a field or thermionic emission sources are typically accelerated to 15 or 20 kV. By applying a negative bias to the sample with respect to the objective lens, the high-energy electrons are decelerated in a cathode lens to the desired energy before arriving at the specimen surface. The electrons reflected from the surface are then reaccelerated and collected using a channeltron. Contrast in LEEM images can arise from changes in electron reflectivity due to variations in crystal orientation, surface composition, structure, and topography.[53] Step height differences can also cause constructive and destructive interference in the reflected beam, yielding a phase contrast. Through the adjustment of the imaging conditions, information

regarding surface roughness, film thickness, domain orientation, and surface composition can be obtained.

LEEM, analogous to TEM, can be operated in bright and dark field modes, where a diffracted beam is selected using a contrast aperture and is used to form an image. In bright field mode, the (0,0) beam is used for imaging, whereas in dark field imaging, a diffracted beam is selected to acquire the images. LEEM can also be operated in other modes: photoemission electron microscopy (PEEM) and mirror electron microscopy (MEM). In PEEM, an ultraviolet or other photon source, rather than an electron beam, illuminates the sample, causing photoemission of electrons that are directed through the objective lens and subsequently form the image. MEM mode involves the use of electrons with $E = 0$ eV with respect to the sample. These electrons do not directly interact with the surface. Instead, they are reflected approximately 100 nm from the surface. Image contrast is due primarily to variations in surface roughness and work function variation.

LEEM is particularly well suited for the study of graphene. Its attractive aspects include the dynamical observation of surface morphology, structural changes, and simultaneous determination of surface electronic structure. Real space information can be obtained from the LEEM images, crystallographic data from low-energy electron diffraction (LEED), and surface work function and layer thickness from electron reflectivity measurements.[54]

All the graphene growth experiments were carried out on (111)-oriented Pd single crystals in an UHV-LEEM system, with a base pressure of 1×10^{-10} Torr. Figure 8 is a schematic representation of the various components that make up the UHV system. In order to achieve UHV necessary for graphene growth, a number of vacuum pumps are utilized, including four

turbomechanical pumps, three ion pumps, and one titanium sublimation pump. Each turbomechanical pump is connected to a rotary vane pump so chamber pressure can be reduced to the necessary operation pressures. Ion pumps are attached to the main chamber as well as the LEEM, which is isolated from the primary chamber. Samples are cleaned by Ar^+ ion sputtering in the preparation chamber. A load-lock system separates the main chamber from the preparation chamber and helps maintain UHV in the main chamber during sample cleaning. Additional samples can be stored in an adjacent chamber, also maintained at UHV.

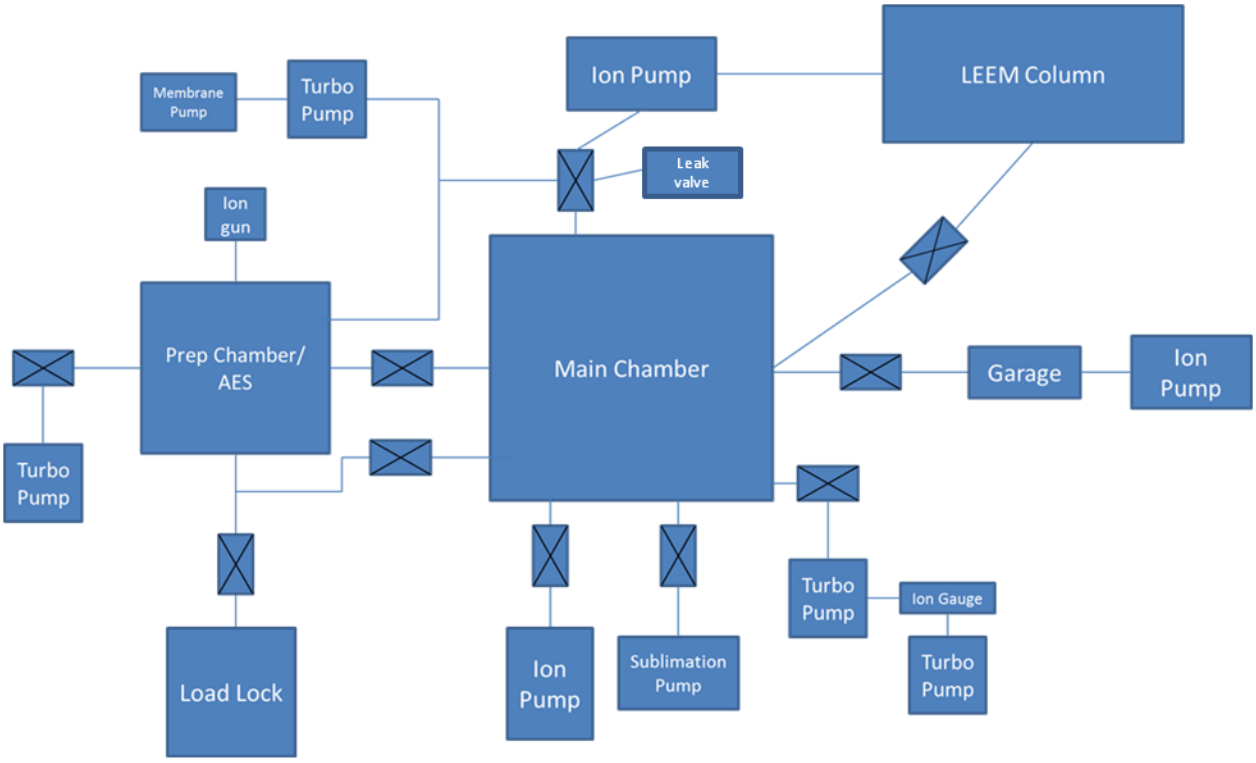

Figure 8. Schematic layout of the UHV LEEM system used for graphene growth experiments.

2.2 Sample Preparation

Prior to the growth experiments, the Pd(111) crystal was first saturated with carbon by annealing at 900 ^{o}C overnight in a tube furnace while flowing a mixture of 90% Ar - 10% CH_4 at 760 Torr. The crystal was then air-transferred to the LEEM system, where the sample was degassed and

cleaned in the preparation chamber by repeated cycles of sputtering with 1.5 keV Ar^+ ions and annealing at 900 ^oC. Sample temperature was monitored through the use of a type-C thermocouple spot welded to a washer flush to the crystal. The samples were heated from the backside using electron beam. After cleaning, the sample was vacuum transferred to the main chamber.

Graphene growth was achieved by first heating the crystal to high temperatures T, for example between 880 ^oC and 960 ^oC, and then cooling to a lower temperature. At T > 880 ^oC, bulk solubility of C in Pd is high (~ 1.4 at.%) and all of the carbon remains in the bulk. Upon cooling, carbon solubility decreases and the excess carbon precipitates out on the surface in the form of graphene. By choosing the appropriate temperature, C solubility in the bulk and hence the thickness of graphene layers on the surface can be precisely controlled. Moreover, this approach enables multiple reproducible growth experiments on the *same* region of interest on the surface, thus minimizing artifacts and is ideal for the accurate determination of the growth kinetics. Bright field LEEM images were acquired at the rate of 2 frames/s while continuously varying the incident electron energy *E* between 0 and 6 eV in steps of 0.2 eV. Typical field of view was 20 μm and pixel resolution in the images was 391 Å/pixel. Selected area LEED patterns were obtained from regions of interest, and were used to identify orientations of graphene domains[55] and surface structure.

As part of my thesis, graphene monolayers were grown both in UHV and in the presence of oxygen. A base pressure of approximately 1 x 10^{-10} Torr was maintained for UHV growths. For growth in presence of oxygen, molecular oxygen was introduced with the aid of a leak valve and the O_2 pressure was varied between UHV and 5 x 10^{-6} Torr.

2.3 Image Processing and Analysis

Time-dependent changes in areas $A(t)$ of graphene domains and image intensities $I(E,t)$ were determined from the LEEM images using Image J, an image processing software. Batching processing of the images was performed using software routines, see appendix I. In order to minimize measurement uncertainties, only the images acquired at E = 6 eV (where graphene domains can be clearly distinguished from the bare Pd regions) were used to extract the $A(t)$ data. $I(E,t)$ values for bare Pd and graphene-covered regions are obtained as the average intensities of all the pixels within selected regions of interest. The batch processing code used for electron reflectivity measurements can be found in appendix II. From each image, intensity data was extracted from at least three different regions and three sizes (195×195 nm^2, 391×391 nm^2, and 586×586 nm^2) and checked for consistency. All the results presented here are representative of my measurements.

In order to obtain work function Φ of the surface, electron reflectivity is plotted versus electron energy E. In these electron reflectivity curves, the electron energy corresponding to a 10% decrease in image intensity is referred to as the electron injection threshold energy and is used to extract work function Φ of the surface by the relation $\Phi_{surface} = \varphi_{surface} + \Phi_{fil}$, where Φ_{fil} is the work function of the electron gun filament.[56] Electron energy values are extrapolated at normalized electron intensity values of 0.9 to obtain the injection energy φ. Calibration of Φ_{fil} is achieved by measuring φ of clean Pd(111), which in my experiments was found to be 2.2 ± 0.1 eV. From the literature value of Φ_{Pd}, 5.3 ~ 5.6 eV,[57] I determined $\Phi_{fil} = \Phi_{Pd} - \varphi$ = 3.1 ~ 3.4 eV. For all calculations of $\Phi_{surface}$ in my experiments, a Φ_{fil} of 3.4 eV was used.

CHAPTER 3: RESULTS AND DISCUSSION

3.1 Monolayer Graphene Growth in Ultra-high Vacuum

Figure 9 shows typical LEEM images acquired in the bright field mode from the Pd(111) crystal during the growth of monolayer graphene as a function of time t at T = 880 ^{o}C. The time t = 0 corresponds to the time at which the sample temperature reaches 880 ^{o}C upon cooling from 960 ^{o}C. Images were obtained at an incident electron energy E = 5 eV. The field of view in the images is 20 μm. In this particular experiment, graphene layer nucleated elsewhere and has grown into the field of view [see Figs. 9a-d]. Note that the image contrast of bare Pd(111) in Figure 9a changes significantly during the growth of monolayer graphene. Surface features, presumably 3D defects, that are visible in the Figure 9a disappear at later times with increased graphene coverage.

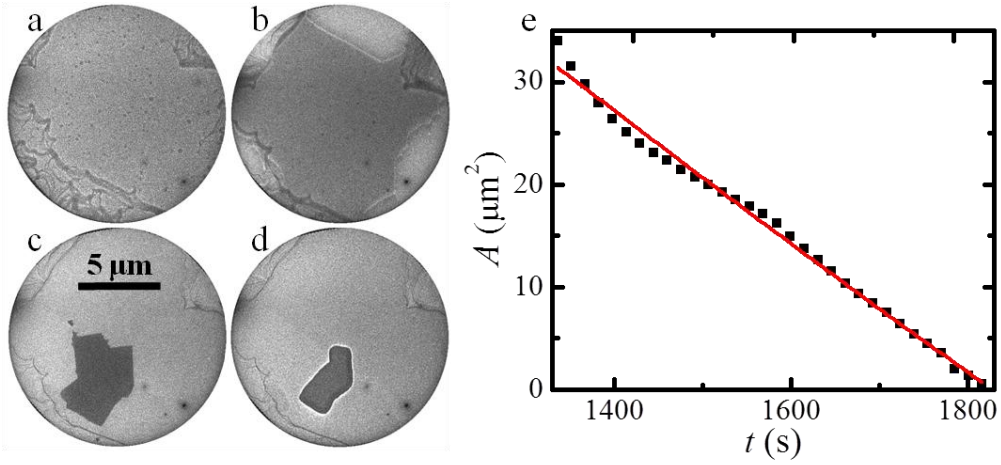

Figure 9. Representative bright-field LEEM images acquired from a Pd(111) sample at times t = (a) 44 s, (b) 831 s, (c) 1330 s, and (d) 1594 s. T = 880 ^{o}C. (e) Plot of bare Pd island area A vs. t (solid squares). Solid red line is the least squares linear fit to the data.

Figure 9e shows the change in bare (graphene-free) Pd area, A with respect to time. A was found to decrease linearly with t, i.e. areal growth rate $\left(\frac{dA}{dt}\right)$ of graphene is constant. Growth of

graphene on the surface requires two basic steps: (i) diffusion of C atoms from the bulk (or subsurface) to the surface and (ii) attachment of the C adatoms at the graphene step edges. For diffusion-controlled growth of graphene, as observed on Ru(0001),[40] graphene domain area was found to change non-linearly with time as $A^2 \propto t$.

The observed constant rate of graphene growth on Pd(111) can be due to one of the following two rate-limiting processes: 1) the attachment of C adatoms at the step edges, or 2) the exchange of intercalated carbon atoms between the graphene-substrate interface and the bulk. In the case where C adatom attachment at the step edges is rate-limiting, A is expected to scale linearly with t if (i) the bulk diffusivity of C atoms is sufficiently high and/or there is an ample supply of C atoms on or near the surface at all times and (ii) there exists a barrier for attachment of C atoms at the Pd or graphene step edges. The former criterion is likely satisfied, as recent experiments[48] have shown that 3D mounds of graphene composed of multiple layers (>10) can be grown readily by lowering the temperature. The latter condition is plausible as the growth of graphene on other metals required the attachment of C atom clusters rather than individual atoms.[39]

For the growth of graphene from intercalated C atoms, under the assumption that the rates of diffusion of carbon to and on the surface as well as the attachment at the graphene edges are fast, flux of C is given by:

$$J \sim (C_{eq}^{B} - C_{eq}^{G}).$$

In the above equation, C_{eq}^{B} is the intercalated C concentration in equilibrium with graphene and C_{eq}^{G} is the intercalated C concentration in equilibrium with the bulk. In this relation, both the concentrations are expected to be independent of time if the bulk C concentration and bulk

diffusivity of C are both significantly high. Thus, $\frac{dA}{dt} \sim J$ is predicted to be constant, consistent with the experimental results. This model is based upon the assumption that the surface C adatoms do not interact with the intercalated C atoms and do not contribute to the growth of graphene. Consequently, the C adatom concentration on bare Pd is isolated from the intercalated C atom concentration.

In order to better understand the observed changes in image contrast, image intensity I is measured as a function of E and t. Figure 10a is a plot of $I/I(t = 0)$ vs. t data for graphene-free Pd extracted from the measurement sequence in Figure 9. Note the decrease in I with increasing t. Figure 10b shows representative electron reflectivity curves (plots of $I/I(E = 0)$ vs. E) measured from bare Pd surfaces during the same experiment at three different times during graphene growth. These results are in contrast with the behavior observed for monolayer graphene grown on Ru(0001), where the threshold energies φ remain constant at all times.

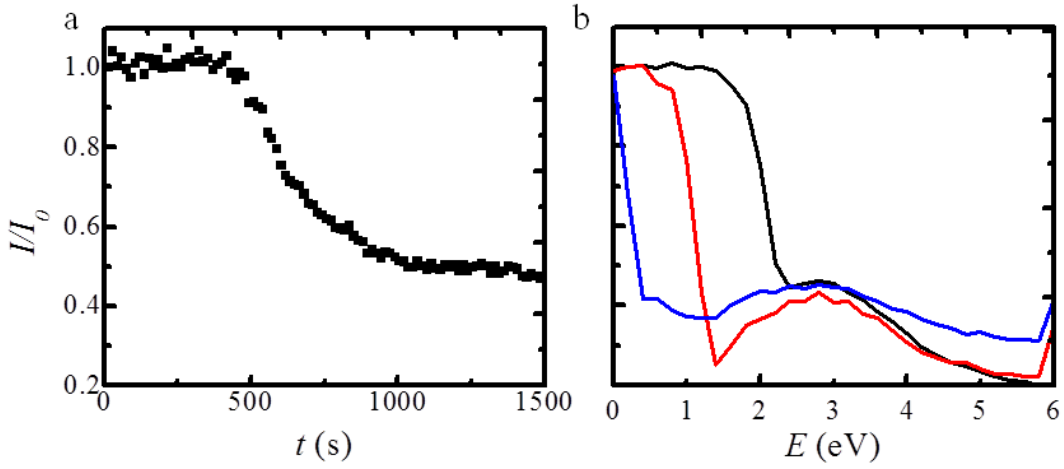

Figure 10. (a) Plot of LEEM image intensity $I/I(t = 0)$ of bare Pd vs. t during monolayer graphene growth. The $I(t)$ data is measured from LEEM images obtained at a constant E = 6 eV. (b) Plot of $I/I(E = 0)$ vs. E for bare Pd at t = 0 s (black), 1272 s (red), and 1613 s (blue). The time taken to acquire each set of $I(E)$ data is 30 s.

Using the methods outlined in section 2.3, work function values Φ_G of graphene-covered and Φ_{Pd} of graphene-free regions were extracted. Figure 11 shows time-dependent variations in Φ_G and Φ_{Pd} values measured from the LEEM images [see Figs. 11b-11d] acquired during the growth immediately followed by dissolution of graphene. The data is collected from the same field of view. Φ_G remains essentially constant at ~ 4.3 eV at all times during graphene growth and dissolution processes. In contrast, Φ_{Pd} decreases from ~ 5.3 eV to ~ 4.5 eV with increasing time at the same growth temperature. And, upon increasing the temperature, as graphene begins to dissolve, Φ_{Pd} increases from ~ 4.2 eV to ~ 4.9 eV. (The difference in the value (4.5 eV) measured at the growth temperature towards the end of the growth and the value (4.2 eV) measured at the beginning of dissolution at higher temperature is likely due to the time elapsed during the temperature change.) In these experiments, the rate of change in Φ_{Pd} depends on both the substrate temperature and time. And, the absolute values of Φ_{Pd} vary with the sample history and the surface morphology in each experiment. The observed decrease (increase) in Φ_{Pd} with time during graphene growth (dissolution) at a given low (high) temperature is a direct indication that the surface or sub-surface composition of graphene-free regions is changing with time and that these changes can be reversed by increasing (decreasing) the temperature.

The relationship between the measured Φ_{Pd} and the carbon atom concentration in the vicinity of the Pd(111) surface can be explained by the accumulation of non-graphitic carbon, either in the form of metastable carbidic phases (Pd_xC) or as C adatoms, in or under the Pd surface during graphene growth. Recent first-principles calculations have suggested that Pd and C can form several carbides of the form Pd_xC, out of which carbides x = 1, 3, and 6 are relatively stable.[58] A separate study has shown that Φ_{Pd} varies with x, of the order of ~ 0.05 eV for Pd_6C and Pd_3C and 0.15 eV for NaCl-structured PdC.[59] However, the carbide phases alone cannot account for the

observed changes in work function (see Figure 11). It can be inferred that in addition to carbides there exist free carbon adatoms on the surface that contribute to observed variations in work function.

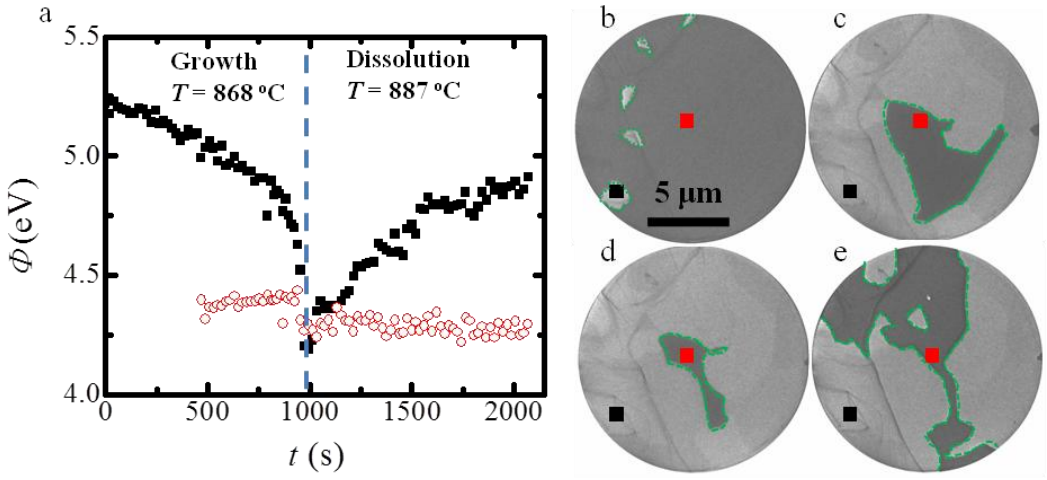

Figure 11. (a) Plot of work functions Φ of graphene-free (■) and graphene-covered (○) Pd surfaces as a function of t during growth at T = 872 °C and during dissolution at T = 887 °C. In this experiment, at t = 0, T = 887 °C. Within 100 s, the sample is cooled to T = 872 °C and held constant. Starting at t ~ 950 s, over a period of 20 s, the T is increased to 887 °C. Associated LEEM images (field of view = 20 μm and E = 6 eV) obtained from the Pd(111) sample during graphene growth at t = (b) 200 s and (c) 954 s, and during dissolution at t = (c) 1100 s and (d) 2000 s. In the images, the darker grey contrast regions outlined by green dotted lines are graphene islands. The Φ values of graphene-free and graphene-covered Pd surfaces are extracted from the solid black square and open red circle regions, respectively.

To substantiate this inference, LEED was used to determine the presence of adatoms on the substrate. Figs. 12a and 12b are typical selected area LEED patterns obtained from graphene-free regions on the Pd sample during graphene growth at 884 °C and after cooling to 37 °C, respectively. At the growth temperature, the only LEED spots that were observed correspond to Pd(111), as shown in Figure 12a. At the lower temperature, additional spots corresponding to an $(\sqrt{3} \times \sqrt{3})$R30° structure [see Figure 12b], characteristic of an ordered C adatom layer, were found. The absence of any additional LEED spots at the graphene growth temperature can be due

either to the lack of ordering or low surface coverages of C adatoms. These results suggest that C adatoms can co-exist with graphene on the Pd surface. Furthermore, DFT studies have shown that increasing C adatom coverages cause a decrease in Φ_{Pd}.[59] These calculations demonstrate that for surface coverages above 50%, changes in Φ_{Pd} are as large as 0.9 eV, providing strong evidence that the changes shown in Figure 11(a) may be a result of high C adatom concentration.

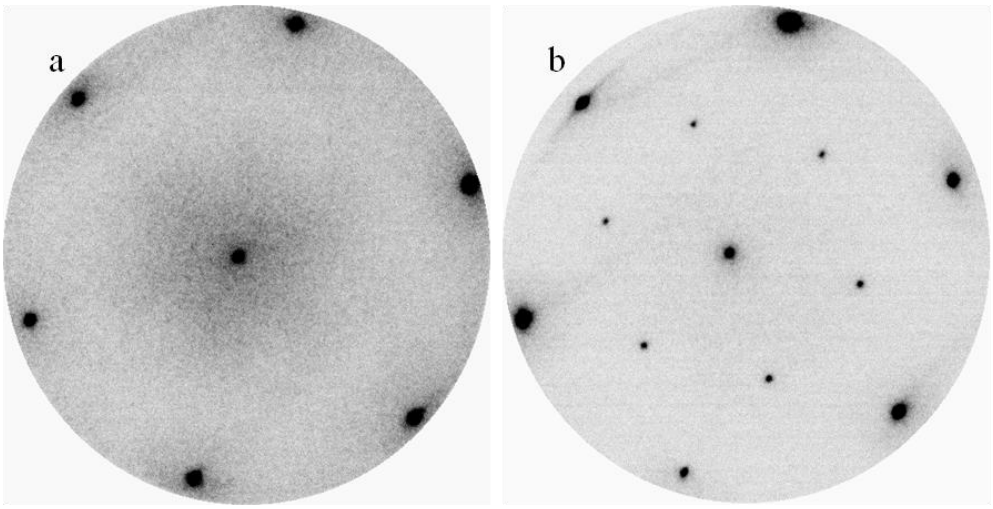

Figure 12. Selected area LEED patterns obtained from the same graphene-free Pd(111) surface (a) during graphene growth at T = 884 ^{o}C and (b) after cooling of the sample to T = 37 ^{o}C.

3.2 Monolayer Graphene Growth in Presence of O_2

In order to investigate the effects of oxygen exposure on monolayer graphene on Pd(111), the work function Φ_{Pd} of bare Pd(111) regions was measured during graphene growth in UHV and in oxygen environments. Figure 13 is a plot of Φ_{Pd} vs. t during monolayer growth of graphene. In this experiment, O_2 was introduced during graphene growth, sequentially increasing from p = 2.5 x 10^{-9} Torr at t = 0 s to p = 5.0 x 10^{-8} Torr at t = 1000 s, 1.0 x 10^{-7} Torr at t = 1100 s, 1.0 x 10^{-6} Torr at t = 1200 s, and 5.0x 10^{-6} Torr at t = 1350 s. Note the gradual change in Φ_{Pd} with time, indicative of a change in surface C adatom concentration on the surface. A similar change in Φ_{Pd}

was also observed during graphene growth in UHV as a result of the increasing adatom concentration, as discussed in section 3.1. While surface carbon can be readily depleted upon exposure to O_2 gas in the form carbon monoxide,[30] in my experiments, it is difficult to distinguish the effects of oxygen on the surface C adatom concentration.

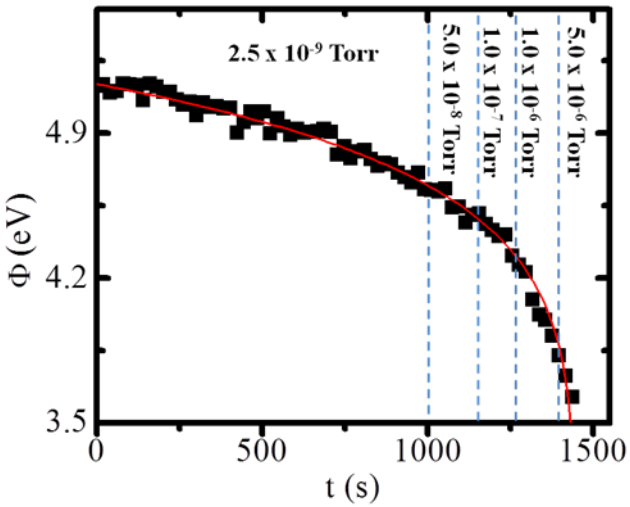

Figure 13: Plot of work function of graphene free regions vs. *t* during graphene growth at *T* = 868 ^{o}C. The dashed lines indicate times at which the O_2 pressures were changed.

In addition to Φ_{Pd} measurements, time dependent changes in area were extracted from the LEEM images. In Figure 14, the change in bare Pd area is plotted as a function of time during graphene growth at two different O_2 pressures. As observed for graphene grown in UHV, the *A* vs. *t* relationship is linear, i.e. $\frac{dA}{dt}$ is constant. However, the growth rate decreases with increasing O_2 pressure. In these experiments, a five-fold increase in the O_2 pressure from 1.0 x 10^{-6} Torr to 5.0 x 10^{-6} Torr resulted in a decrease of growth rate from ~ 0.07 $\mu m^2/s$ to ~ 0.03 $\mu m^2/s$. The reduction in graphene growth rate can be a result of etching of: 1) C adatoms on the surface, 2) intercalated C atoms, and 3) C from the graphene layers. Since the time-dependent decrease in Φ_{Pd} during graphene growth both in UHV and in the presence of oxygen are qualitatively

similar, it is likely that the oxygen has little effect on the surface C concentration. However, additional experiments are required to confirm this conclusion. The fact that time-dependent changes in graphene area follows the same linear behavior, i.e. constant $\frac{dA}{dt}$, irrespective of the oxygen pressure indicates that the growth mechanism is unaffected by the introduction of oxygen. That is, graphene growth is primarily due to the intercalated C atoms. The observed decrease in growth rate with increasing oxygen pressure can then be attributed to etching of intercalated C atoms and/or graphene layers. The latter is possible and has been observed for graphene on Ir(111) and Ru(0001) systems, where small amounts of oxygen ($p = 5 \times 10^{-9}$ Torr) was sufficient to etch away the graphene layers.[30] Yet another possible mechanism by which the growth rate can be influenced by oxygen exposure involves intercalation of oxygen atoms to the graphene-substrate interface. It is not clear yet which of these processes control the graphene growth in the presence of oxygen and additional experiments are required to fully understand the observed behavior.

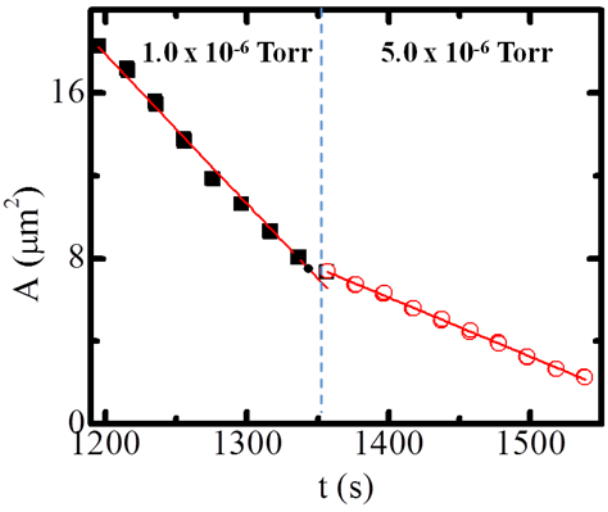

Figure 14. Plot of bare Pd island area *A* vs. *t* at *T* = 868 °C. Dashed line indicates the time at which O_2 pressure was increased from 1.0 x 10^{-6} Torr to 5.0 x 10^{-6} Torr.

CHAPTER: 4 SUMMARY

As part of my thesis work, I grew monolayer graphene via segregation of carbon dissolved in a Pd(111) crystal and used LEEM to study the growth kinetics. Electron reflectivity and time dependent changes in area were extracted from the data collected in real time as a function of temperature and oxygen pressure. Using data obtained from the LEEM images, the areal growth rate of monolayer graphene was found to be constant. This behavior is different from the kinetics of graphene growth on other metals, such as Ru and Ir.

To explain my observations, two different growth models are suggested: growth by adatom attachment and growth by intercalated carbon. Further work is necessary to validate these models. A key objective looking ahead is the understand the roles of C adatoms and intercalated C atom behavior during growth. Measurements of the concentration of these two carbon sources as functions of time, temperature, and O_2 pressure would shed light onto which of the two growth mechanism operate on Pd(111).

Work function measurements obtained during the growth and dissolution show that Pd(111) surface composition changes with time. Selected area LEED studies have shown that a dense ordered phase is present on graphene-free Pd at low temperatures, but is not detectable at growth temperatures. Insight into relation between this dense adsorbed phase and the proposed growth models should be revealed with addition experimental work.

The effect of oxygen on graphene growth kinetics was also investigated. Work function values measured while varying O_2 pressures are qualitatively similar to those observed during the growth of graphene in UHV. The absence of any clear changes in Φ_{Pd} during O_2 exposure suggests that C adatom concentration is unaffected by oxygen. The reduction in growth rate in

this experiment is likely a result of oxygen interaction with intercalated C atoms or a direct etching of the graphene layers. Future studies featured an O_2 exposure to graphene islands with constant area would reveal if etching occurs or if oxygen is interacting with intercalated carbon atoms. Furthermore, such conditions would also identify if any changes to Φ_{Pd} occur with the introduction of oxygen.

APPENDIX I

IMAGE J SCRIPT FOR AREA MEASUREMENT

```
path="C:\\Users\\SingMok\\Documents\\Work\\Lab\\LEEM 9011\\";
ex_date="090711";
filename="o";
//Define file directory

run("Set Scale...", "distance=512 known=20 pixel=1 unit=micron");
//Reset image scale from pixel to micron.

for (number=2666; number<3565; number=number+31) {
if (number<10) i="00"+number;
else if (number>=10 && number<100) i="0"+number;
else i=number;
//Define file name loop.

run("Raw...",     "open=["+path+ex_date+"\\"+ex_date+filename+"\\"+ex_date+filename+i+".dat]
image=[16-bit Unsigned] width=512 height=512 offset=392 number=1 gap=0 little-endian");
//Open .dat files

makeRectangle(179, 235, 142, 173);
run("Crop");
run("8-bit");
//Draw region of interest. Values here are for reference and may vary.

run("Analyze Particles...", "size=10-Infinity circularity=0.00-1.00 show=Outlines display
exclude clear");
saveAs("BMP",path+ex_date+"\\"+ex_date+filename+"\\area_data\\outline of
"+ex_date+filename+i+".bmp");
//Measure area in region of interest.

f=File.openAsString(path+ex_date+"\\"+ex_date+filename+"\\area_data\\"+ex_date+filename+"
_area.txt");
g=File.open(path+ex_date+"\\"+ex_date+filename+"\\area_data\\"+ex_date+filename+"_area.txt
");
print(g, f);
print(g, number+","+Area+","+perimeter+"\n");
//Save measured data to system and to a preexisting .txt file in directory.

File.close(g);
close();
}
```

APPENDIX II

IMAGE J SCRIPT FOR ELECTRON REFLECTIVITY MEASUREMENT

```
path="C:\\Users\\Sing Mok\\Documents\\Work\\Lab\\LEEM 9011\\";
ex_date="090711";
filename="o";
//Define file directory

run("Set Scale...", "distance=512 known=20 pixel=1 unit=micron");
//Reset image scale from pixel to micron.

for (number=30; number<3719; number= number + 31) {
if (number<10) i="00"+number;
else if (number>=10 && number<100) i="0"+number;
else i=number;
//Define file name loop.

run("Raw...", "open=["+path+ex_date+"\\"+ex_date+filename+"\\"+ex_date+filename+i+".dat]
image=[16-bit Unsigned] width=512 height=512 offset=392 number=1 gap=0 little-endian");
//Open .dat files

makeRectangle(230, 344, 10, 10);
run("Measure");
//Draw region of interest. Values here are for reference and may vary.

intensity=getResult("IntDen", 0);
run("Clear Results");
//Measure image intensity values

f=File.openAsString(path+ex_date+"\\"+ex_date+filename+"_IV.txt");
g=File.open(path+ex_date+"\\"+ex_date+filename+"_IV.txt");
print(g, f);
print(g, number+","+intensity+"\n");
//Save measured data to system and to a preexisting .txt file in directory.

File.close(g);
close();
}
```

REFERENCES

1 A. K. Geim and K. S. Novoselov, "*The rise of graphene*," Nat Mater **6** (3), 183-191 (2007).

2 A. C. Neto, F. Guinea, and N. M. R. Peres, "*Drawing conclusions from graphene*," Phys World **19** (11), 33-37 (2006).

3 A. H. Castro Neto, F. Guinea, N. M. R. Peres, K. S. Novoselov, and A. K. Geim, "*The electronic properties of graphene*," Rev Mod Phys **81** (1), 109-162 (2009).

4 T. Ando, "*Exotic electronic and transport properties of graphene*," Physica E **40** (2), 213-227 (2007).

5 P. Sutter, J. T. Sadowski, and E. A. Sutter, "*Chemistry under Cover: Tuning Metal-Graphene Interaction by Reactive Intercalation*," J Am Chem Soc **132** (23), 8175-8179 (2010).

6 E. Granas, J. Knudsen, U. A. Schroder, T. Gerber, C. Busse, M. A. Arman, K. Schulte, J. N. Andersen, and T. Michely, "*Oxygen Intercalation under Graphene on Ir(111): Energetics, Kinetics, and the Role of Graphene Edges*," Acs Nano **6** (11), 9951-9963 (2012).

7 K. I. Bolotin, K. J. Sikes, Z. Jiang, M. Klima, G. Fudenberg, J. Hone, P. Kim, and H. L. Stormer, "*Ultrahigh electron mobility in suspended graphene*," Solid State Commun **146** (9-10), 351-355 (2008).

8 M. Y. Han, B. Ozyilmaz, Y. B. Zhang, and P. Kim, "*Energy band-gap engineering of graphene nanoribbons*," Phys Rev Lett **98** (20), 206805 (2007).

9 K. I. Bolotin, K. J. Sikes, J. Hone, H. L. Stormer, and P. Kim, "*Temperature-dependent transport in suspended graphene*," Phys Rev Lett **101** (9), 096802 (2008).

10 J. S. Moon, D. Curtis, S. Bui, M. Hu, D. K. Gaskill, J. L. Tedesco, P. Asbeck, G. G. Jernigan, B. L. VanMil, R. L. Myers-Ward, C. R. Eddy, P. M. Campbell, and X. Weng, "*Top-Gated Epitaxial Graphene FETs on Si-Face SiC Wafers With a Peak Transconductance of 600 mS/mm*," Ieee Electr Device L **31** (4), 260-262 (2010).

11 S. Bae, H. Kim, Y. Lee, X. F. Xu, J. S. Park, Y. Zheng, J. Balakrishnan, T. Lei, H. R. Kim, Y. I. Song, Y. J. Kim, K. S. Kim, B. Ozyilmaz, J. H. Ahn, B. H. Hong, and S. Iijima, "*Roll-to-roll production of 30-inch graphene films for transparent electrodes*," Nat Nanotechnol **5** (8), 574-578 (2010).

12 O. V. Yazyev and S. G. Louie, "*Electronic transport in polycrystalline graphene*," Nat Mater **9** (10), 806-809 (2010).

13 A. W. Tsen, L. Brown, M. P. Levendorf, F. Ghahari, P. Y. Huang, R. W. Havener, C. S. Ruiz-Vargas, D. A. Muller, P. Kim, and J. Park, "*Tailoring Electrical Transport Across Grain Boundaries in Polycrystalline Graphene*," Science **336** (6085), 1143-1146 (2012).

14 K. S. Kim, Y. Zhao, H. Jang, S. Y. Lee, J. M. Kim, K. S. Kim, J. H. Ahn, P. Kim, J. Y. Choi, and B. H. Hong, "*Large-scale pattern growth of graphene films for stretchable transparent electrodes*," Nature **457** (7230), 706-710 (2009).

15 K. S. Novoselov, A. K. Geim, S. V. Morozov, D. Jiang, Y. Zhang, S. V. Dubonos, I. V. Grigorieva, and A. A. Firsov, "*Electric field effect in atomically thin carbon films*," Science **306** (5696), 666-669 (2004).

16 X. S. Li, W. W. Cai, J. H. An, S. Kim, J. Nah, D. X. Yang, R. Piner, A. Velamakanni, I. Jung, E. Tutuc, S. K. Banerjee, L. Colombo, and R. S. Ruoff, "*Large-Area Synthesis of High-Quality and Uniform Graphene Films on Copper Foils*," Science **324** (5932), 1312-1314 (2009).

17 Q. K. Yu, J. Lian, S. Siriponglert, H. Li, Y. P. Chen, and S. S. Pei, "*Graphene segregated on Ni surfaces and transferred to insulators*," Appl Phys Lett **93** (11), 113103 (2008).

18 I. Forbeaux, J. M. Themlin, and J. M. Debever, "*Heteroepitaxial graphite on 6H-SiC(0001): Interface formation through conduction-band electronic structure*," Phys Rev B **58** (24), 16396-16406 (1998).

19 J. Borysiuk, J. Soltys, R. Bozek, J. Piechota, S. Krukowski, W. Strupinski, J. M. Baranowski, and R. Stepniewski, "*Role of structure of C-terminated 4H-SiC(000(1)over-bar) surface in growth of graphene layers: Transmission electron microscopy and density functional theory studies*," Phys Rev B **85** (4), 045426 (2012).

20 S. Oida, F. R. McFeely, J. B. Hannon, R. M. Tromp, M. Copel, Z. Chen, Y. Sun, D. B. Farmer, and J. Yurkas, "*Decoupling graphene from SiC(0001) via oxidation*," Phys Rev B **82** (4), 041411 (2010).

21 Luxmi, N. Srivastava, G. He, R. M. Feenstra, and P. J. Fisher, "*Comparison of graphene formation on C-face and Si-face SiC {0001} surfaces*," Phys Rev B **82** (23), 235406 (2010).

22 R. M. Tromp and J. B. Hannon, "*Thermodynamics and Kinetics of Graphene Growth on SiC(0001)*," Phys Rev Lett **102** (10), 063046 (2009).

23 S. Bhaviripudi, X. T. Jia, M. S. Dresselhaus, and J. Kong, "*Role of Kinetic Factors in Chemical Vapor Deposition Synthesis of Uniform Large Area Graphene Using Copper Catalyst*," Nano Lett **10** (10), 4128-4133 (2010).

24 P. Sutter, J. T. Sadowski, and E. Sutter, "*Graphene on Pt(111): Growth and substrate interaction*," Phys Rev B **80** (24), 245411 (2009).

25 P. W. Sutter, J. I. Flege, and E. A. Sutter, "*Epitaxial graphene on ruthenium*," Nat Mater **7** (5), 406-411 (2008).

26 J. Coraux, A. T. N'Diaye, M. Engler, C. Busse, D. Wall, N. Buckanie, F. J. M. Z. Heringdorf, R. van Gastel, B. Poelsema, and T. Michely, "*Growth of graphene on Ir(111)*," New J Phys **11**, 023006 (2009).

27 A. B. Preobrajenski, M. L. Ng, A. S. Vinogradov, and N. Martensson, "*Controlling graphene corrugation on lattice-mismatched substrates*," Phys Rev B **78** (7), 073401 (2008).

28 A. Y. Tontegode, "*Carbon on Transition-Metal Surfaces*," Prog Surf Sci **38** (3-4), 201-429 (1991).

29 W. F. Chung and M. S. Altman, "*Step contrast in low energy electron microscopy*," Ultramicroscopy **74** (4), 237-246 (1998).

30 E. Starodub, N. C. Bartelt, and K. F. McCarty, "*Oxidation of Graphene on Metals*," J Phys Chem C **114** (11), 5134-5140 (2010).

31 Peter Sutter, Peter Albrecht, Xiao Tong, and Eli Sutter, "*Mechanical Decoupling of Graphene From Ru(0001) by Interfacial Reaction with Oxygen*," J Phys Chem C **12** (117), 6320-6324 (2013).

32 C. Oshima and A. Nagashima, "*Ultra-thin epitaxial films of graphite and hexagonal boron nitride on solid surfaces*," J Phys-Condens Mat **9** (1), 1-20 (1997).

33 S. Marchini, S. Gunther, and J. Wintterlin, "*Scanning tunneling microscopy of graphene on Ru(0001)*," Phys Rev B **76** (7), 075429 (2007).

34 T. A. Land, T. Michely, R. J. Behm, J. C. Hemminger, and G. Comsa, "*Stm Investigation of Single Layer Graphite Structures Produced on Pt(111) by Hydrocarbon Decomposition*," Surf Sci **264** (3), 261-270 (1992).

35 J. C. Shelton, H. R. Patil, and J. M. Blakely, "*Equilibrium Segregation of Carbon to a Nickel (111) Surface - Surface Phase-Transition*," Surf Sci **43** (2), 493-520 (1974).

36 S. Nie, W. Wu, S. R. Xing, Q. K. Yu, J. M. Bao, S. S. Pei, and K. F. McCarty, "*Growth from below: bilayer graphene on copper by chemical vapor deposition*," New J Phys **14**, 093028 (2012).

37 G. A. Lopez and E. Mittemeijer, "*The solubility of C in solid Cu*," Scripta Mater **51** (1), 1-5 (2004).

38 X. S. Li, W. W. Cai, L. Colombo, and R. S. Ruoff, "*Evolution of Graphene Growth on Ni and Cu by Carbon Isotope Labeling*," Nano Lett **9** (12), 4268-4272 (2009).

39 E. Loginova, N. C. Bartelt, P. J. Feibelman, and K. F. McCarty, "*Evidence for graphene growth by C cluster attachment*," New J Phys **10**, 093026 (2008).

40 E. Loginova, N. C. Bartelt, P. J. Feibelman, and K. F. McCarty, "*Factors influencing graphene growth on metal surfaces*," New J Phys **11**, 063046 (2009).

41 K. F. McCarty, P. J. Feibelman, E. Loginova, and N. C. Bartelt, "*Kinetics and thermodynamics of carbon segregation and graphene growth on Ru(0001)*," Carbon **47** (7), 1806-1813 (2009).

42 D. Teschner, J. Borsodi, A. Wootsch, Z. Revay, M. Havecker, A. Knop-Gericke, S. D. Jackson, and R. Schlogl, "*The roles of subsurface carbon and hydrogen in palladium-catalyzed alkyne hydrogenation*," Science **320** (5872), 86-89 (2008).

43 F. N. Xia, V. Perebeinos, Y. M. Lin, Y. Q. Wu, and P. Avouris, "*The origins and limits of metal-graphene junction resistance*," Nat Nanotechnol **6** (3), 179-184 (2011).

44 P. Franke and D. Neuschütz, "*Binary Systems Supplement 1, Phase Diagram, Phase Transition Data, Integral and Partial Quantities of Alloys*," Landolt-Bornstein; Springer: Berlin, (2007).

45 C. Gong, G. Lee, B. Shan, E. M. Vogel, R. M. Wallace, and K. Cho, "*First-principles study of metal-graphene interfaces*," J Appl Phys **108** (12), 123711 (2010).

46 S. Y. Kwon, C. V. Ciobanu, V. Petrova, V. B. Shenoy, J. Bareno, V. Gambin, I. Petrov, and S. Kodambaka, "*Growth of Semiconducting Graphene on Palladium*," Nano Lett **9** (12), 3985-3990 (2009).

47 Y. Murata, E. Starodub, B. B. Kappes, C. V. Ciobanu, N. C. Bartelt, K. F. McCarty, and S. Kodambaka, "*Orientation-dependent work function of graphene on Pd(111)*," Appl Phys Lett **97** (14), 143114 (2010).

48 Y. Murata, S. Nie, A. Ebnonnasir, E. Starodub, B. B. Kappes, K. F. McCarty, C. V. Ciobanu, and S. Kodambaka, "*Growth structure and work function of bilayer graphene on Pd(111)*," Phys Rev B **85** (20), 063046 (2012).

49 B. B. Kappes, A. Ebnonnasir, S. Kodambaka, and C. V. Ciobanu, "*Orientation-dependent binding energy of graphene on palladium*," Appl Phys Lett **102** (5), 051606 (2013).

50 E. Bauer, "*The Resolution of the Low-Energy Electron Reflection Microscope*," Ultramicroscopy **17** (1), 51-56 (1985); W. Telieps and E. Bauer, "*An Analytical Reflection and Emission Uhv Surface Electron-Microscope*," Ultramicroscopy **17** (1), 57-65 (1985).

51 E. Bauer, "*LEEM basics*," Surf Rev Lett **5** (6), 1275-1286 (1998).

52 R. M. Tromp and M. C. Reuter, "*Imaging with a low-energy electron microscope*," Ultramicroscopy **50**, 171-178 (1992).

53 E. Bauer, "*Low-Energy-Electron Microscopy*," Rep Prog Phys **57** (9), 895-938 (1994).

54 H. Hibino, H. Kageshima, F. Maeda, M. Nagase, Y. Kobayashi, and H. Yamaguchi, "*Microscopic thickness determination of thin graphite films formed on SiC from quantized oscillation in reflectivity of low-energy electrons*," Phys Rev B **77** (7) (2008).

55 K. F. McCarty, "*Imaging the crystallization and growth of oxide domains on the NiAl(110) surface*," Surf Sci **474** (1-3), L165-L172 (2001).

56 B. Unal, Y. Sato, K. F. McCarty, N. C. Bartelt, T. Duden, C. J. Jenks, A. K. Schmid, and P. A. Thiel, "*Work function of a quasicrystal surface: Icosahedral Al-Pd-Mn*," J Vac Sci Technol A **27** (5), 1249-1250 (2009).

57 H. L. Skriver and N. M. Rosengaard, "*Surface-Energy and Work Function of Elemental Metals*," Phys Rev B **46** (11), 7157-7168 (1992).

58 N. Seriani, F. Mittendorfer, and G. Kresse, "*Carbon in palladium catalysts: A metastable carbide*," J Chem Phys **132** (2), 063046 (2010).

59 H. S. Mok, A. Ebnonnasir, Y. Murata, S. Nie, N. C. Bartelt, K. F. McCarty, C. V. Ciobanu, and S. Kodambaka, "*Growth Kinetics of Monolayer Graphene on Pd(111)*," (2013).